



# Gaussian random field generator for simulating partially coherent undulator radiation

ANDREI TREBUSHININ,<sup>1,\*</sup> GIANLUCA GELONI,<sup>1</sup> YAKOV RAKSHUN,<sup>2</sup> AND SVITOZAR SERKEZ<sup>1,3</sup>

<sup>1</sup>European XFEL, 4, Holzkoppel Street, 22869 Schenefeld, Germany

<sup>2</sup>Budker Institute of Nuclear Physics, 11, Lavrentieva Avenue, 630090 Novosibirsk, Russia

<sup>3</sup>e-mail: svitozar.serkez@xfel.eu

\*Corresponding author: andrei.trebushinin@xfel.eu

Received 11 April 2022; revised 3 June 2022; accepted 15 June 2022; published 22 July 2022

Wavefront propagation codes play pivotal roles in the design of optics at synchrotron radiation sources. However, they usually do not account for the stochastic behavior of the radiation field originating from shot noise in the electron beam. We propose a computationally efficient algorithm to calculate a single statistical realization of partially coherent synchrotron radiation fields at a given frequency. This field can be consequently propagated from the source position downstream through an optical beamline to the sample position. The proposed algorithm relies on a method for simulating Gaussian random fields. We initially generate the radiation field as Gaussian white noise and then restrict it in both real and inverse space domains for a given radiation size and divergence. We exploit the assumption of quasi-homogeneity of the source. However, we show that the method is applicable with reasonable accuracy outside of this assumption. The proposed algorithm is consistent with other well-established approaches, and, in addition, it possesses an advantage in terms of computational efficiency. It can be extended to other types of sources that follow Gaussian statistics. Finally, the demonstration of the algorithm is well suited for educational purposes. © 2022 Optica Publishing Group under the terms of the Optica Open Access Publishing Agreement

<https://doi.org/10.1364/OPTICA.460902>

## 1. INTRODUCTION

Advance in the design of storage-ring-based synchrotron radiation sources [1,2] led to a reduction in electron beam emittance down to the diffraction limit for a wide range of photon wavelengths  $\lambda$  such that

$$\epsilon_{x,y} < \sigma_r' \sigma_r = \frac{\lambda}{4\pi}, \quad (1)$$

where  $\sigma_r'$  and  $\sigma_r$  are the natural divergence and size of radiation at the source emitted by a filament, respectively, i.e., with zero transverse size. Radiation from diffraction-limited light sources possesses full transverse coherence. However, even brand new fourth-generation light sources are only partially coherent at high enough photon energies.

The process of designing beamlines for modern synchrotron radiation sources involves simulations of partially coherent radiation and its propagation through an optical system. Ray-tracing codes, such as in [3–5] and references within [6], have often served this aim. However, these codes assume poor spatial coherence, while already at third-generation light sources, the radiation in vertical direction is diffraction limited at photon energies of the order of 1 keV. In this case, the usefulness of ray-tracing becomes limited. One needs to accurately account for diffraction effects using wave optics approaches or, alternatively, come up with a solution to adapt ray-tracing for this purpose, such as a hybrid approach [6].

The wave optics approach allows to straightforwardly account for the effects related to fully coherent radiation. Nevertheless, the case of partially coherent radiation remains a sophisticated problem. Various authors have covered the theoretical basis of the statistical properties of synchrotron radiation in many publications [7–13]. In [7], a statistical optics approach is applied to the case of third-generation synchrotron radiation sources. The characteristics of synchrotron radiation heavily depend on the presence of shot noise in an electron beam. Because of this, amplitudes and phases of the radiation exhibit stochastic fluctuations. In other words, radiation field distributions change from realization to realization, and to obtain statistically meaningful intensities and correlation functions, one needs to average over a statistical ensemble so that the framework of statistical optics [14] becomes quite natural. Here we consider undulator sources that are mostly widespread. Approaches for simulating partially coherent undulator radiation are proposed in several codes and in plenty of publications. Based on the framework of statistical optics, one can consider propagating the cross-spectral density function of the electric field by exploiting coherent mode decomposition methods; see [15–19]. This method requires significant computational resources, as discussed in [20]. Nevertheless, the authors of [21] report improved CPU efficiency of the coherent mode decomposition method.

An alternative type of method is based on Monte-Carlo-like simulations. If one is interested in radiation field intensity

at a given frequency, one can calculate radiation from separate electrons. Then, one can simply sum up intensities from these individual electrons; this procedure is valid when the length of an electron beam is long compared to the radiation wavelength, which is always the case for conventional use of synchrotrons. One of the most well-known wave optics simulation toolkits, Synchrotron Radiation Workshop (SRW) [22–24], uses a Monte-Carlo-like approach for treating partially coherent radiation in simulations [25–31]. We discuss this approach in Section 3.B.

When computational resources allow for it, one can also use a Monte-Carlo-like approach where the electric fields from particles—not the intensities—are summed up to form a single realization of the synchrotron radiation field. We discuss the field addition method (FAM) in Section 3.A with the aim to facilitate understanding of the theory, Section 2. In this approach, instead of dealing with ensemble-averaged quantities, one considers separate realizations of a stochastic process, similar to what is done, for example, in free electron laser (FEL) simulations [32].

The algorithm we propose here follows a similar way for simulating partially coherent synchrotron radiation. It relies on the generation of instances of the stochastic process, instead of dealing with ensemble-averaged quantities such as correlation functions or averaged intensities. The method we propose is based on a Gaussian random field (GRF) generator. In practice, we restrict complex Gaussian noise by the effective size and divergence of the radiation field. Introducing Gaussian noise, we effectively emulate the contribution of shot noise accounting for all electrons at once. As a result, the algorithm provides the complex amplitude of a multimode field of undulator radiation, suitable for propagation through a beamline. We call this method the synchrotron emission rapid evaluator (SERVAL) and present its description along with a comparative analysis with Monte-Carlo-like approaches. Also, we demonstrate the application of SERVAL in the case of a simple focusing system with an exit pupil. SERVAL is part of the Ocelot [33] toolkit, which was developed for start-to-end simulations of FEL and synchrotron light sources.

## 2. THEORETICAL BACKGROUND ON UNDULATOR RADIATION STATISTICAL PROPERTIES

### A. Qualitative Reasoning

Undulator radiation has an intrinsic stochastic structure caused by random distribution of electrons in a volume of 6D phase space. This distribution follows shot noise statistics, as the number of electrons located in the finite volume of the electron beam phase space is *discrete* and *random*. This shot noise is imprinted in the radiation structure. It manifests itself as longitudinal and transverse spikes in the radiation pulse as illustrated in Figs. 1 and 2. By its nature, those fields follow the same statistics as *thermal light*: both are described in terms of Gaussian random processes [14].

The duration of a temporal spike of undulator radiation field in the  $t$  domain is coherence time at a given harmonic. The transverse spiky structure may be explored with a monochromator that is capable of resolving a single spike in the radiation spectrum. For example, in [34,35],  $\Delta E/E = 8 \times 10^{-9}$  relative resolution was reached at energy 14.41 keV, which is  $\Delta\omega_m \sim 2 \times 10^{11}$  Hz in absolute units. This allowed to resolve a single spike in the spectrum with absolute width of  $2\pi/\sigma_T \sim 2 \times 10^{11}$  Hz. In the case of an ideal setup (perfect monochromator and detector), a two-dimensional detector will show a transverse spiky structure in the

radiation pulse, as illustrated in Figs. 1 and 2. Note that resolving one spike in the frequency domain is mathematically equivalent to studying the emission at a specific frequency  $\omega$ .

In contrast with thermal sources, which are fully incoherent and whose coherent spot size at the source is about the radiation wavelength, undulator sources are partially coherent, and they exhibit a coherent spot size equal to the single-electron diffraction size. For the case of thermal light, the relation of the spiky structure in the far zone with the source size is described by Van Cittert-Zernike theorem [36,37]. This theorem relates the cross-spectral density in the far zone with the intensity distribution at the source via Fourier transform. For undulator radiation, this theorem is applied only to the special case of quasi-homogeneous sources. To assess the coherence properties of the source, one should compare the natural size and divergence of the radiation from a single electron with the size and divergence of the electron beam. Applicability of Van Cittert-Zernike theorem to undulator radiation was thoroughly reviewed in [7] and discussed in the following sections of this paper. For further use, here we introduce two dimensionless parameters to describe the radiation size and divergence of the single electron with respect to those of the electron beam:

$$D_{x,y} = \frac{\sigma_{x',y'}^2}{\lambda/(2\pi L_w)}, \quad N_{x,y} = \frac{\sigma_{x,y}^2}{\lambda L_w/(2\pi)}, \quad (2)$$

where  $\sigma_{x',y'}$  and  $\sigma_{x,y}$  are the electron beam divergence and size in each direction, respectively. The source has a large number of spikes if  $N \gg 1$  and  $D \gg 1$  in both planes. In the case of single electron radiation,  $N$  and  $D$  become vanishingly small, resulting in a single spike.

### B. Mathematical Description

The radiation field from an undulator generated by an electron beam with  $N_e$  electrons can be written as the sum of the fields (our mathematical notation coincides with that in [7]) from each individual electron. We represent the field of undulator radiation in the  $\omega\vec{r}$  domain by a function  $\bar{E}(z, \vec{r}, \omega)$ , where the radiation field is considered at a given frequency  $\omega$ .  $\bar{E}(z, \vec{r}, \omega)$  is related with the field  $E(z, \vec{r}, t)$  in the  $t\vec{r}$  domain by inverse Fourier transform. The radiation from the whole electron beam is written as

$$\bar{E}_b(z, \vec{r}, \omega) = \sum_{k=1}^{N_e} \bar{E}(\vec{\eta}_k, \vec{l}_k, z, \vec{r}, \omega) e^{i\omega t_k}, \quad (3)$$

where  $z$  is the distance from the undulator center to the observation plane, and  $\vec{r}$  is transverse coordinates in the observation plane. Here we consider a mono-energetic electron beam. With Monte-Carlo-like approaches, this can be easily accounted in Eq. (3) by just adding into the formulas the Lorentz factor of the  $k$ th electron,  $\gamma_k$ .

The  $k$ th electron has its transverse offset  $\vec{l}_k$  and deflection angle  $\vec{\eta}_k$  from the reference trajectory inside an undulator, and an arrival time  $t_k$  with respect to the reference electron. In the  $\omega\vec{r}$  domain, the arrival time contributes to the expression of the electric field as an additional phase factor  $\exp(i\omega t_k)$ . Quantities  $\vec{\eta}_k$ ,  $\vec{l}_k$  are assumed to follow Gaussian distributions  $f_\eta(\vec{\eta})$  and  $f_l(\vec{l})$ , with zero mean values and variances  $\sigma_{x',y'}, \sigma_{x,y}$ . Approximation of the beams with transverse Gaussian shapes is very applicable for storage rings.

Having Eq. (3), one may check that  $\bar{E}_b$  is a circular complex Gaussian random variable, [7], (for fixed  $z$ ,  $\vec{r}$ , and  $\omega$ ), which is a

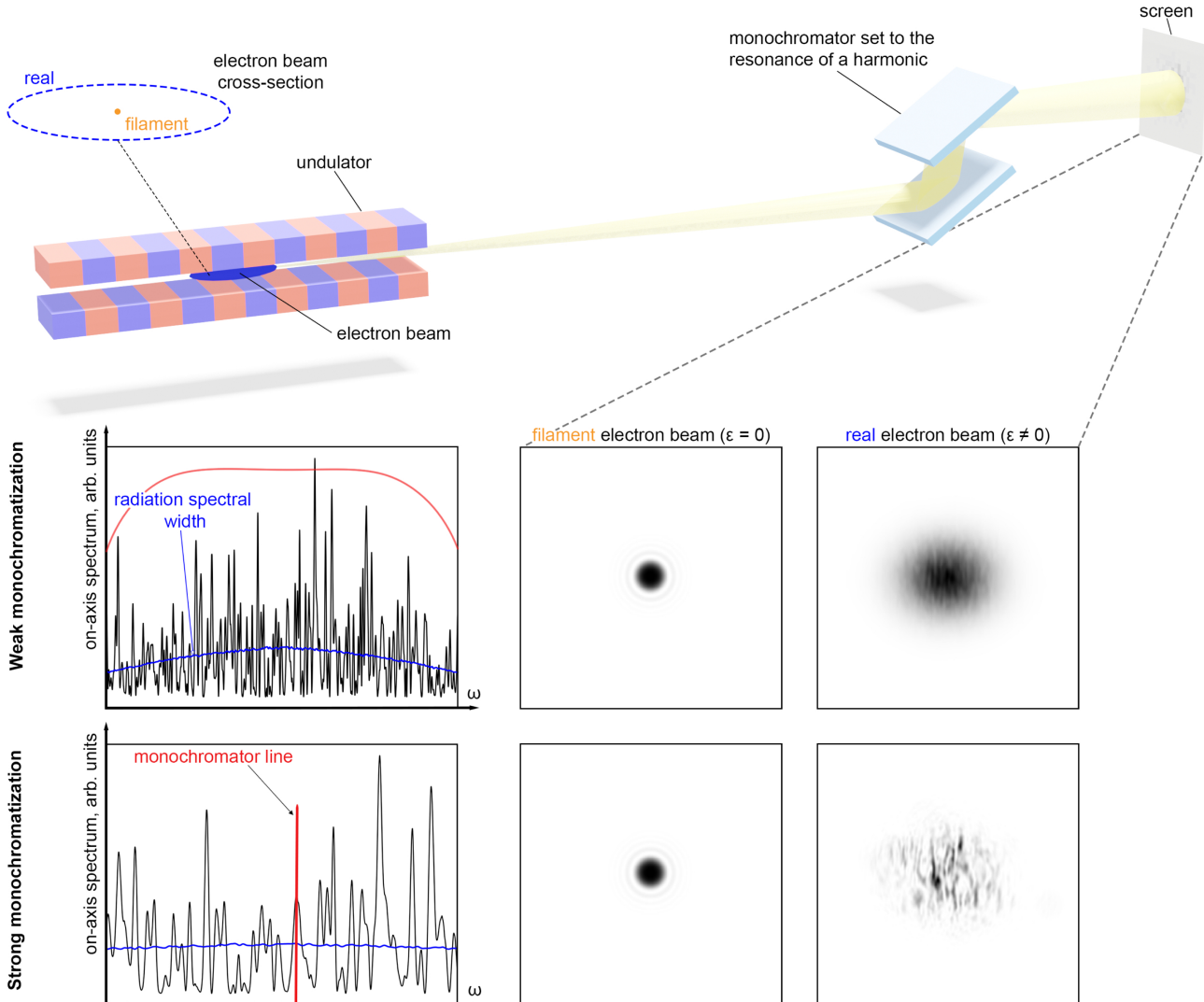


**Fig. 1.** Spiky structure of synchrotron radiation. We compare radiation from a filament electron beam and from an electron beam with non-zero emittance. Figures on the left contain a single realization of spectrum (black lines) and ensemble-averaged spectrum (blue lines). Red lines represent the resolving power of monochromators. The plot on the top row illustrates a typical monochromatization incapable of resolving spectral spikes. To obtain the intensity observed at a detector (after single passage of the electron beam), one needs to average over these frequencies/realizations. This is justified, as the different spikes in the spectrum are not correlated in the time or, correspondingly, frequency domain. The bottom plot represents the resolving power of a monochromator that allows to resolve a single spectral spike of undulator radiation revealing its transverse spiky structure. The four figures on the right represent transverse intensity distribution upon monochromatization.

fundamental property of thermal sources as well as synchrotron radiation. This fact will be used in the proposed algorithm.

Returning to the longitudinal direction, an electron arrival time  $t_k$  also follows Gaussian distribution  $f_t(t_k)$  with standard deviation  $\sigma_T$  for most cases. Here  $\sigma_T$  is the duration of the electron beam. The electron beam length  $c\sigma_T$  is almost always much larger than the radiation wavelength ( $\omega\sigma_T \gg 1$ ). Here we do not consider coherent synchrotron radiation (CSR) effect. This fact implies that the phase  $\omega t_k$  in Eq. (3) is uniformly distributed over the interval  $(0, 2\pi)$ . Also, radiation fields from individual electrons are not correlated with each other.

In general, synchrotron radiation is a non-stationary process. However, in a realistic case, the natural spectral width of undulator radiation at fundamental harmonic resonance is of order  $\omega_r/N_w$ , where  $\omega_r$  is the resonance frequency, and  $N_w$  is the number of undulator periods. The relation  $\omega_r\sigma_T/N_w \gg 1$  still holds {see the parameters estimation in [7], paragraph after Eq. (10)}. This

relation means that the longitudinal width of the spikes is much smaller than the radiation bandwidth. Having this, one can conclude that the source is quasi-stationary and derive a relation {Eq. (19) in [7]} that is an analogous to Wiener–Khinchin theorem. Quasi-stationary approximately means that the number of spikes in the longitudinal direction is large and they have the same width across the spectrum. We refer to this case as a “long” electron beam approximation.

### 1. Cross-Spectral Density Function

As remarked before, at conventional synchrotrons, a “long” electron beam approximation applies, and under this assumption, we can express the spatial coherence separately from the longitudinal correlation, via the *cross-spectral density function*  $G$  at fixed frequency  $\omega$  {see, e.g., Eq. (12) in [7]}:

$$G(z, \vec{r}_1, \vec{r}_2, \omega) \equiv \langle \bar{E}(\vec{\eta}, \vec{l}, z, \vec{r}_1, \omega) \bar{E}^*(\vec{\eta}, \vec{l}, z, \vec{r}_2, \omega) \rangle, \quad (4)$$

where  $\langle \dots \rangle$  denotes averaging over the ensemble of fields  $\bar{E}(\vec{\eta}_k, \vec{l}_k, z, \vec{r}, \omega)$  emitted by electrons with the deflections  $\vec{\eta}_{1,\dots,N_e}$  and offset  $\vec{l}_{1,\dots,N_e}$  at fixed frequency  $\omega$ . Then, it is customary to define a normalized version of  $G$ , the *spectral degree of coherence*  $g(z, \vec{r}_1, \vec{r}_2)$ , as

$$g(z, \vec{r}_1, \vec{r}_2) = \frac{G(z, \vec{r}_1, \vec{r}_2)}{\sqrt{\langle |\bar{E}(\vec{\eta}, \vec{l}, z, \vec{r}_1)|^2 \rangle \langle |\bar{E}(\vec{\eta}, \vec{l}, z, \vec{r}_2)|^2 \rangle}}. \quad (5)$$

Starting from here, we will omit  $\omega$  in the equations for brevity of the notation.

## 2. Quasi-Homogeneous Sources

Quasi-homogeneity is the transverse equivalent of quasi-stationarity. It means that at different transverse positions across the radiation beam intensity  $\bar{I}(z, \vec{r})$  transverse spikes have the same “shape.” It allows us to factorize cross-spectral density of the virtual source (located at  $z = 0$ ):

$$G(0, \vec{r}, \Delta \vec{r}) = \bar{I}(0, \vec{r}) g(0, \Delta \vec{r}), \quad (6)$$

where we introduced two new variables:  $\vec{r} = (\vec{r}_1 + \vec{r}_2)/2$  and  $\Delta \vec{r} = (\vec{r}_1 - \vec{r}_2)$ .

Quasi-homogeneous sources are characterized by a special relation that is strictly related to the van Cittert–Zernike theorem [36,37] between source-intensity distribution  $\bar{I}(0, \vec{r})$  and spectral degree of coherence in the far zone  $g(z_0, \Delta \theta)$ , where  $z_0$  denotes the position in the far zone. Despite the word “spectral,” this degree of coherence determines coherence properties in *real* or *inverse* space domain at given frequency  $\omega$ , which is implied. Namely, these two quantities form a Fourier pair. Note that the factorization presented in Eq. (6) is possible if

- (i) intensity of the radiation at the source varies slowly at the scale of coherence length (i.e., large number of transverse spikes);
- (ii) transverse coherence length does not depend on the transverse position (i.e., similar shape of transverse spikes).

## 3. SIMULATING UNDULATOR RADIATION BY AN ELECTRON BEAM DIRECTLY

We introduce two different approaches to simulate radiation field from an undulator at a given frequency emitted by an electron beam with finite emittance.

The first one—*FAM*—is to sum up radiation fields (amplitudes and phases) of all individual electrons in the beam, as suggested in Eq. (3). This would allow one to construct a single realization of the field at given radiation frequency. Conventional monochromator resolution effectively sums up intensities from neighboring spectral spikes, as can be deduced from Fig. 1. Looking at single-shot pulses downstream, a conventional monochromator is equivalent to averaging over numerous realizations.

In the second approach—*intensity addition method* (IAM)—radiation fields from each electron are propagated to a sample location, and afterwards, one sums up their intensity distributions. This method relies on the assumption of a long electron beam, discussed in Section 2, and is easily applicable to wavelengths below visible light.

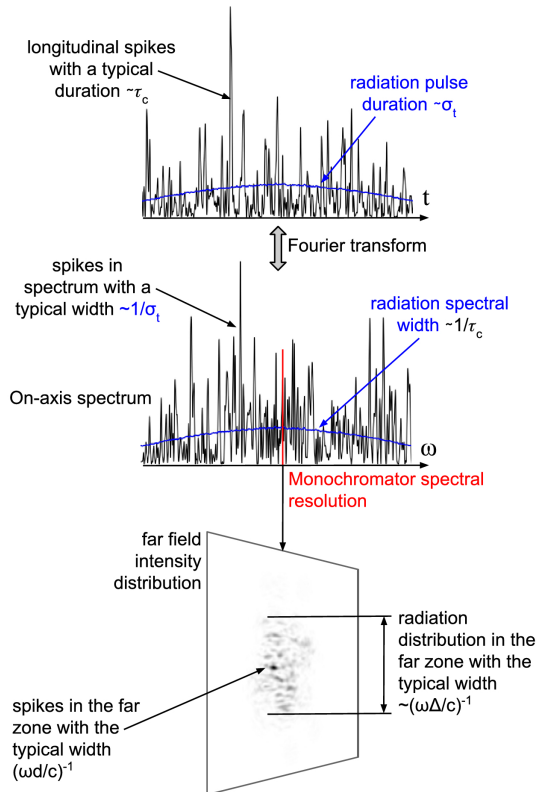


**Fig. 2.** Illustration of the spiky structure of a specific harmonic of undulator radiation. The red line indicates a resolving power of the monochromator. Black line represents an on-axis radiation spectrum and its time domain, and blue line shows the ensemble-averaged values. The bottom figure represents the transverse spiky structure of undulator radiation upon strong monochromatization (red line). Here we tacitly imply the quasi-homogeneity and quasi-stationarity of the source.  $d$  and  $\Delta$  represent source size and typical spike size at the source, respectively,  $\tau_c$  is the coherence length,  $\sigma_t$  is the typical radiation pulse duration,  $\omega$  denotes radiation carrier frequency, and  $c$  is speed of light.

Of course, in both approaches, summing up over all electrons in the beam is not computationally feasible; however, electrons can be modeled with a smaller number of macroparticles with proportionally larger charges.

As mentioned, the IAM using macroparticles is implemented in well-known code SRW.

### A. Field Addition Method

Summing up fields of  $N_e$  electrons according to Eq. (3) will result in a single statistical realization of monochromatized undulator radiation with transverse spiky structure as illustrated in Fig. 1.

The observed intensity upon averaging over realizations (with an ideal monochromator) is

$$I_\omega = \left\langle \left| \sum_{k=1}^{N_e} \bar{E}(\vec{\eta}_k, \vec{l}_k, z, \vec{r}) \exp(i\omega t_k) \right|^2 \right\rangle, \quad (7)$$

where the transverse ensemble-averaged intensity distribution converges and becomes “smooth.” This approach is illustrated in Fig. 3 and provides the most straightforward solution to the problem of simulating partially coherent synchrotron radiation.

Also with this method, one can simulate *coherent synchrotron radiation* (CSR) by summing all fields emitted by the electrons

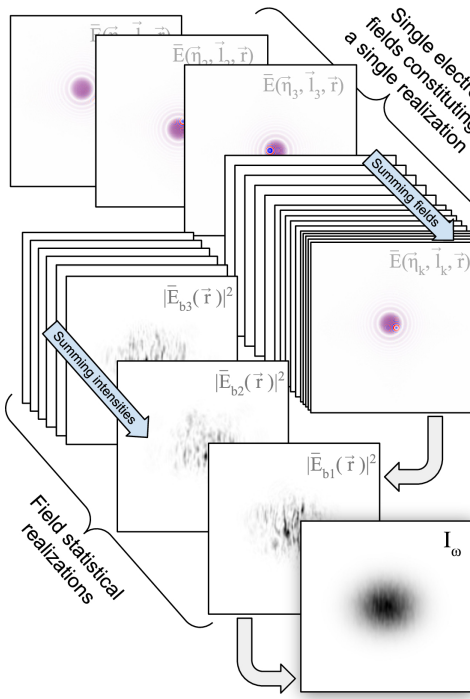


**Fig. 3.** Scheme of the field addition method. Radiation from macroparticles  $\bar{E}(\vec{\eta}_k, \vec{l}_k, \vec{r})$  is summed up to compose a single field realization  $\bar{E}_{1b}(\vec{r})$ . Each  $\bar{E}(\vec{\eta}_k, \vec{l}_k, \vec{r})$  is displayed with false color (positive values with red and negative with blue) to show the amplitude and phase of the radiation. After averaging over different field realizations  $\bar{E}_b(\vec{r})$ , one obtains the resulting intensity.

in phase  $\omega t_k$  (pancake beam approximation) or any other phase distribution allowing to account for the sizes of the electron beam comparable to the radiation wavelength, e.g., THz radiation.

We note that both numbers—number of bunches  $N_b$  and number of electrons  $N_e$ —have a direct physical meaning. However, the number of electrons in a beam is immense. To deal with this in simulations, one needs to exploit a concept of macroparticles  $N_p$ . This number is relatively low, of order of hundreds, but sufficient for obtaining statistically meaningful intensities and correlations. Depending on the degree of coherence, this number may vary: a poorer degree of coherence requires a higher number of realizations for obtaining statistically meaningful results, i.e., one macroparticle is enough to simulate a zero-emittance beam. The optimal amount of macroparticles should be found empirically when increasing the quantity leads to a diminishing change in the simulation results.

The time needed for such calculations can be estimated as the time required to calculate  $N_e$  instances of the fields (for each electron), and afterward averaging over  $N_b$  field realizations  $\bar{E}_b$ . To sum up, if  $\tau_{calc}$  is the time needed for calculating the field from a single electron, then the time needed for the resulting ensemble-averaged intensity is  $T_{calc} = \tau_{calc} \cdot N_e \cdot N_b$ .

## B. Intensity Addition Method

In the case of a long electron beam, the calculation time can be shortened by knowing that the electron arrival times  $t_k$  are not correlated with each other. Because of this, radiation from different electrons is also not correlated. This means that when we rewrite the ensemble-averaged intensity in Eq. (7) as

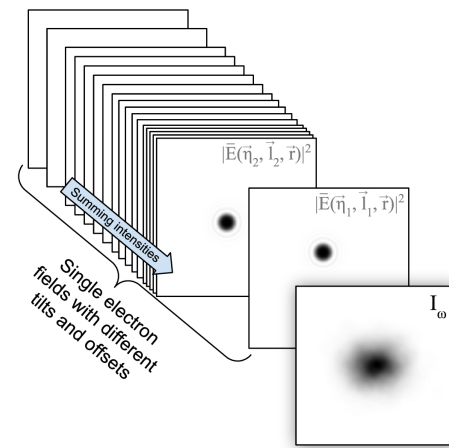


**Fig. 4.** Scheme of the intensity addition method. Having a “long” electron beam, one sums up intensities to obtain the resulting intensity distribution after propagating radiation from each macroparticle through a beamline. Computationally, fields from single electrons are saved in cache memory as different slices of an array (as schematically depicted). These slices then are used to perform beam propagation simulations.

$$I_\omega = \left\langle \sum_{k=1}^{N_e} \bar{E}(\vec{\eta}_k, \vec{l}_k, z, \vec{r}) \bar{E}^*(\vec{\eta}_k, \vec{l}_k, z, \vec{r}) \right\rangle + \left\langle \sum_{k=1}^{N_e} \sum_{n=1, k \neq n}^{N_e} \bar{E}(\vec{\eta}_k, \vec{l}_k, z, \vec{r}) \bar{E}^*(\vec{\eta}_n, \vec{l}_n, z, \vec{r}) \times \exp[i\omega(t_k - t_n)] \right\rangle, \quad (8)$$

the second term vanishes after averaging over the statistical ensemble. The sum over  $N_e$  electrons in the first term in Eq. (8) is equal to an integral over the transverse electron beam phase space (smooth) distribution functions of offsets  $f_l(\vec{l})$  and deflections  $f_\eta(\vec{\eta})$ :

$$I_\omega = \left\langle \sum_{k=1}^{N_e} |\bar{E}(\vec{\eta}_k, \vec{l}_k, z, \vec{r})|^2 \right\rangle = N_e \iint_{\mathbb{R}^4} f_l(\vec{l}) f_\eta(\vec{\eta}) |\bar{E}(\vec{\eta}, \vec{l}, z, \vec{r})|^2 d\vec{l} d\vec{\eta}, \quad (9)$$

which gives us the radiation distribution. Averaging over the ensemble reduces to a sum of  $N_e$  single electrons, which provides a way to evaluate the integral:

$$I_\omega \propto \sum_{k=1}^{N_e} |\bar{E}(\vec{\eta}_k, \vec{l}_k, z, \vec{r})|^2. \quad (10)$$

Moreover, one can calculate the cross-spectral density according to Eq. (4). This approach, based on Eq. (10), grants a powerful and time-efficient method for calculating partially coherent synchrotron radiation.

The time needed for calculation becomes just  $T_{calc} = \tau_{calc} \cdot N_e$ . We call this approach, for simplicity, IAM. We depict the scheme of this method in Fig. 4.

## 4. SERVAL ALGORITHM

In this section, we will show that it is possible to obtain results of the FAM described in Section 3.A within a convenient computational

time and under the assumption of quasi-homogeneity of the source using an alternative approach. This algorithm—SERVAL—simulates the stochastic properties of synchrotron radiation that are imprinted in each pulse due to the shot noise in the electron beam. It requires the electron beam to be long, which is actually a non-restrictive assumption in most cases at synchrotrons. We will present this algorithm analytically, showing its strict validity in the case of quasi-homogeneous sources. We also discuss deviations from this approximation and present the application of SERVAL for simulating a beamline.

### A. Algorithm Description

We shape the transverse distribution of the field from an undulator as a GRF in a manner similar to those mathematically described in [38], explained in simple words in [39], and exploited in imitating spectra and power distributions of FEL in the linear regime in [33,40].

The SERVAL field at the center of an undulator ( $z = 0$ ) can be written in the following form:

$$\phi(\vec{r}) = \mathcal{F}^{-1} \left\{ \sqrt{\hat{I}(\vec{\theta})} \mathcal{F} \left\{ \sqrt{\bar{I}(\vec{r}')} \mathcal{W}(\vec{r}') \right\} (\vec{\theta}) \right\} (\vec{r}), \quad (11)$$

where  $\mathcal{F}\{\cdot\}(\vec{\theta})$  and  $\mathcal{F}^{-1}\{\cdot\}(\vec{r})$  are direct and inverse Fourier transforms, respectively, and  $\mathcal{W}(\vec{r}) = X(\vec{r}) + iY(\vec{r})$  is complex Gaussian white noise, where  $X(\vec{r})$ ,  $Y(\vec{r})$  follow the normal distribution with a mean equal to zero and variance equal to unity. Finally,

$$\bar{I}(\vec{r}) = |\bar{E}_b(0, \vec{r})|^2 = \int_{\mathbb{R}^2} f_l(\vec{l}) |\bar{E}(\vec{\eta}, \vec{l}, 0, \vec{r})|^2 d\vec{l}, \quad (12)$$

$$\hat{I}(\vec{\theta}) = |\hat{E}_b(0, \vec{\theta})|^2 = \int_{\mathbb{R}^2} f_\eta(\vec{\eta}) |\hat{E}(\vec{\eta}, \vec{l}, 0, \vec{\theta})|^2 d\vec{\eta} \quad (13)$$

are the intensity distributions of the radiation from the whole electron beam in  $\vec{r}$  domain and inverse-spatial  $\vec{\theta}$  domain, correspondingly. The fields  $\bar{E}(\vec{\eta}, \vec{l}, 0, \vec{r})$  and  $\hat{E}(\vec{\eta}, \vec{l}, 0, \vec{\theta})$  are calculated with a help of Eq. (39) and Eq. (40) from [41]. The physical idea behind Eq. (11) is that the resulting field  $\phi(\vec{r})$  should follow Gaussian statistics and obey the correct first order cross-spectral density function  $g(0, \vec{r}_1, \vec{r}_2)$  under the quasi-homogeneous approximation, as we show in Appendix A. Following Eq. (11), the proposed algorithm consists of four steps: (i) creating complex Gaussian white noise, (ii) constraining it by radiation distribution in the spatial domain at the source location, (iii) Fourier transform to inverse-spatial domain, and (iv) constraining the resulting field in the inverse-spatial domain.  $\vec{r}$  and  $\vec{\theta}$  are assumed to be uncorrelated. We discuss these steps in more detail below:

- (i) Creating complex Gaussian white noise  $\mathcal{W}(\vec{r}_n) = X(\vec{r}_n) + iY(\vec{r}_n)$  in spatial domain.
- (ii) Constraining the complex Gaussian white noise by multiplication of the effective distribution of the radiation at the source expressed by Eq. (12). The result of this step is depicted in Fig. 5(b).
- (iii) Fourier transforming to the inverse-spatial domain [Fig. 6(a)]. At this stage, we have a fully incoherent light source bounded in space akin to a *thermal light source*.

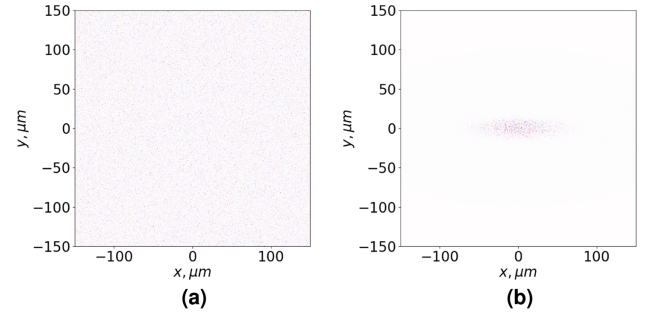


**Fig. 5.** Intensity of complex Gaussian white noise in spatial domain before (a) and after (b) constraining by the effective field size.

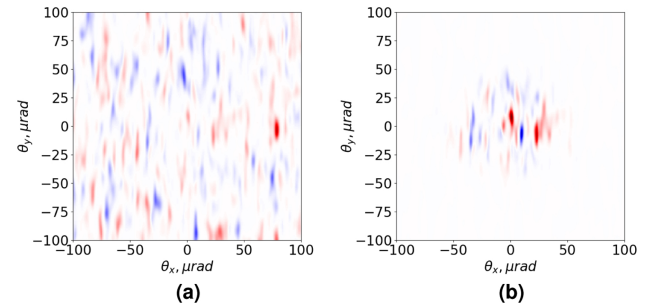


**Fig. 6.** Angular intensity distribution of the field before (a) and after (b) applying radiation divergence constraints.

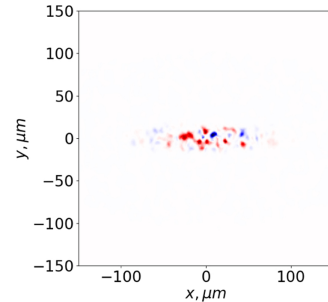


**Fig. 7.** Radiation distribution at the source in real space.

- (iv) Constraining the inverse-spatial distribution in Fig. 6(a) by multiplication with the effective radiation divergence following Eq. (13). This field is ready for propagation through free space, as the free-space propagator works in the inverse-space domain.

After an inverse Fourier transform of the field in Fig. 6(b) back to real space, one obtains the intensity distribution at the source, presented in Fig. 7.

As a result, Figs. 7 and 6(b) depict a single realization of undulator radiation distribution at the source (in the center of the undulator cell), seen through a monochromator capable of resolving beyond the width of a single spike in the frequency domain.

SERVAL yields a radiation field at a given frequency (similar to what other codes do: SRW, mode decomposition algorithm, etc.). Nevertheless, if one needs to simulate transverse radiation distribution downstream a typical monochromator (encompassing numerous spikes), one simply generates single realizations at

slightly different frequencies within the monochromator bandwidth as illustrated in Fig. 1. To obtain the intensity observed at a detector, one needs to average over these frequencies/realizations. This is justified, as the different modes in the spectrum are not correlated (in either  $t$  or, correspondingly,  $\omega$  domain). The computational efficiency of the proposed algorithm may be estimated considering the steps involved: generate  $N_x \cdot N_y$  realizations of  $W(r_n)$ , and carry out two multiplications by constraints and two Fourier transforms. We present a speed test where we compare SERVAL with direct simulation approaches in Appendix B. As we found, using a common laptop, SERVAL performs two orders of magnitude faster compared to the FAM and two times faster than the IAM. However, this result may vary depending on the hardware and programming environment used.

## B. Underlining Assumptions and Approximations

As anticipated in Section 2, and demonstrated in Appendix A, SERVAL is mathematically well-founded for quasi-homogeneous sources, where the cross-spectral density at the source factorizes [Eq. (6)]. This is a strong restriction. In Appendix A, we show to which extent we can apply SERVAL when quasi-homogeneity (large number of spikes) does not hold. We found that our method is satisfactorily applicable if a source is not strictly quasi-homogeneous.

When using SERVAL, we consider single-cell undulators: the single source must have only one waist. This basically implies no quadrupoles, phase shifters, etc., in the magnetic structure of the insertion device. For a magnetic structure with imperfections, one can calculate the intensity distributions from a filament beam [Eqs. (12) and (13)] numerically for a given magnetic structure and then convolve them with the electron beam phase space. If we simulate radiation with SERVAL, the effects of the electron beam emittance (along with energy spread) are accounted for in  $\bar{I}(\vec{r})$  and  $\hat{I}(\vec{\theta})$  [Eq. (11)].

Under these assumptions, SERVAL accurately calculates synchrotron radiation pulses with computational advantages over direct methods. The SERVAL algorithm is not exclusively restricted to undulator sources, as  $\bar{I}(\vec{r})$  and  $\hat{I}(\vec{\theta})$  do not impose any additional restrictions except quasi-homogeneity. Thus, this GRF generator can be used to simulate the stochastic properties of other types of radiation sources.

## 5. APPLICATION OF THE SERVAL ALGORITHM FOR WAVEFRONT PROPAGATION SIMULATIONS

In this section, we present an application of SERVAL for simulating the electromagnetic field emitted by an undulator and its propagation through a beamline using the Ocelot toolkit. To illustrate SERVAL performance outside of its applicability region, we set the electron beam parameters such that they, strictly speaking,

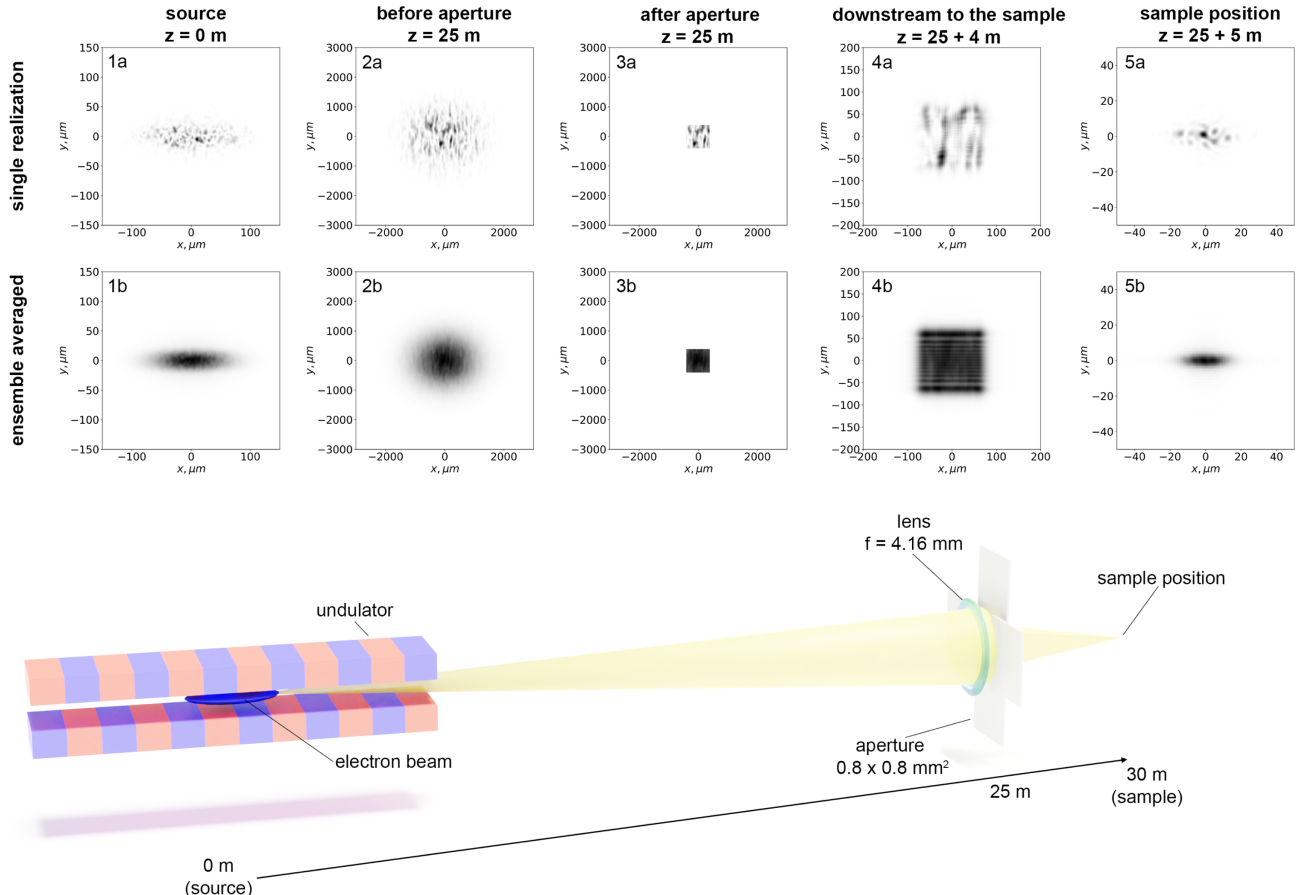


**Fig. 8.** Optical scheme assumed for simulation. Here we propagate radiation at the given frequency, which is why *no monochromator* is presented in the beamline scheme. Left to right: undulator, thin lens with focal distance 4.16 m combined with  $0.8 \times 0.8 \text{ mm}^2$  aperture, both located at 25 m downstream from the center of the undulator. The lens re-imagines the radiation at the sample, located 5 m downstream. (1a)–(5a) and (1b)–(5b) illustrate simulated evolution of radiation distribution. In the top row, we depict single realization shots, and in the bottom row, averaged intensity distributions.

**Table 1.** Assumed Undulator Parameters

$E_{ph}$ , [eV]	$\lambda_w$ , [mm]	Periods
2167	18.	200

**Table 2.** Assumed Electron Beam Parameters

$E$ , [GeV]	$\sigma_x$ , [ $\mu\text{m}$ ]	$\sigma_y$ , [ $\mu\text{m}$ ]	$\sigma_{x'}$ , [ $\mu\text{rad}$ ]	$\sigma_{y'}$ , [ $\mu\text{rad}$ ]
3	38	4.7	25	20

do not follow the approximation of quasi-homogeneity. In the presented simulation, the resulting number of spatial radiation spikes is relatively small. The applicability of SERVAL is discussed in detail in Appendix A.

We consider a simple optical system consisting of a radiation source (undulator), an aperture, and a focusing element (see Fig. 8). The undulator and the electron beam parameters are presented in Tables 1 and 2.

These electron beam parameters correspond to  $N_x = 4.4$ ,  $N_y = 0.07$  and  $D_x = 24.7$ ,  $D_y = 15.8$  according to the definition in Eq. (2).

In Fig. 8, we present radiation intensity distributions of SERVAL-generated field at different positions upon propagation through the simple optical scheme. In this simulation, we propagate *monochromatic realization* of the radiation field, which is why we do not depict the monochromator in the figure. We show both single realization and ensemble-averaged distributions. In this simulation, we used a transverse mesh of  $601 \times 601$  pixels $^2$  and averaged over 401 statistical realizations of the field, which converges towards routinely observable smooth distributions. We calculate the intensity distribution at the source and present it in Figs. 8(1a) and 8(1b), then propagate this radiation downstream the beamline using a free-space propagator over 25 m [Figs. 8(2a) and 8(2b)]. Afterwards, we cut this radiation with a  $0.8 \times 0.8$  mm $^2$  aperture [Figs. 8(3a) and 8(3b)] and, using a thin lens with focal distance  $f = 4.16$  m, focus the radiation down to the sample. To show the diffraction effect that takes place after aperturing, we present the intensity distribution after 4 m of free-space propagation downstream the lens in Figs. 4(a) and 4(b). Upon aperturing at the sample position, we observe a reduction in the number of spikes in the radiation structure. Note that due to higher coherence in the vertical direction, the diffraction pattern is much more pronounced. We present the demagnified image of the source in [Figs. 8(5a) and 8(5b)].

Here we note that averaging over statistical realizations is equivalent to observing the intensity distributions through a conventional monochromator. This can be explained by the fact that common monochromator resolution is still much broader than spike width. One may find further reasoning on this in [7].

We note that considering the electron beam size, we observe more spikes in the horizontal direction than in the vertical one. The typical spike size corresponds to the transverse coherence length. Results of propagating radiation modeled with SERVAL reveals the main aspects of partially coherent radiation and its propagation. Generation of each realization and its propagation in Ocelot took a couple of seconds using a laptop. Of course, such a radiation field can be propagated with other numerical codes such as SRW involving more complex optical elements, however with a benefit of processing multimode fields.

## 6. CONCLUSION

In this paper, we propose a novel computationally efficient algorithm, SERVAL, for simulating partially coherent synchrotron radiation emitted by an undulator at a specific harmonic. The proposed method is based on generating a GRF followed by application of constraints in real and inverse space domains. The result exhibits multimode structure that qualitatively corresponds to a radiation “slice” along the radiation pulse or that could be observed experimentally upon extreme monochromatization.

The algorithm yields a radiation field at the source position, which is usually in the middle of the undulator. One can propagate this field through an optical beamline to the sample location by conventional methods and codes for coherent radiation propagation. The proposed algorithm may be exploited for educational purposes when explaining the basics of coherence.

## APPENDIX A: SERVAL REGION OF APPLICABILITY

### 1. Analytical Treatment

In this appendix, we show explicitly that under the assumption of quasi-homogeneity, the SERVAL algorithm can be used to simulate undulator radiation. First, we will show that the SERVAL field cross-spectral density function coincides with that of the electric field originated from the undulator.

The SERVAL field produced by the GRF generator is written as

$$\phi(\vec{r}) = \mathcal{F}^{-1} \left\{ \sqrt{\hat{I}(\vec{\theta})} \mathcal{F} \left\{ \sqrt{\bar{I}(\vec{r}') \mathcal{W}(\vec{r}')} \right\} (\vec{\theta}) \right\} (\vec{r}). \quad (\text{A1})$$

Then the cross-spectral density function is the following:

$$\begin{aligned} \langle \phi(\vec{r}_1) \phi^*(\vec{r}_2) \rangle &= \left\langle \iint_{\mathbb{R}^4} e^{-2\pi i \{(\vec{r}_1 \cdot \vec{\theta}_1) - (\vec{r}_2 \cdot \vec{\theta}_2)\}} \sqrt{\hat{I}(\vec{\theta}_1)} \hat{I}(\vec{\theta}_2) \right. \\ &\quad \times \iint_{\mathbb{R}^4} e^{2\pi i \{(\vec{r}'_1 \cdot \vec{\theta}_1) - (\vec{r}'_2 \cdot \vec{\theta}_2)\}} \sqrt{\bar{I}(\vec{r}'_1) \bar{I}(\vec{r}'_2)} \\ &\quad \left. \times \mathcal{W}(\vec{r}'_1) \mathcal{W}^*(\vec{r}'_2) d\vec{r}'_1 d\vec{r}'_2 d\vec{\theta}_1 d\vec{\theta}_2 \right\rangle, \end{aligned} \quad (\text{A2})$$

where  $(\cdot)$  denotes a dot product. The field  $\phi(\vec{r})$  is taken at the source position, i.e., center of the undulator. We bring averaging over an ensemble  $\langle \dots \rangle$  inside the integral and take the integral over  $\vec{r}'$ , where we account for the relation  $\langle \mathcal{W}(\vec{r}'_1) \mathcal{W}^*(\vec{r}'_2) \rangle = \delta(\vec{r}'_1 - \vec{r}'_2)$ :

$$\begin{aligned} \langle \phi(\vec{r}_1) \phi^*(\vec{r}_2) \rangle &= \iint_{\mathbb{R}^4} e^{-2\pi i \{(\vec{r}_1 \cdot \vec{\theta}_1) - (\vec{r}_2 \cdot \vec{\theta}_2)\}} \sqrt{\hat{I}(\vec{\theta}_1)} \hat{I}(\vec{\theta}_2) \\ &\quad \times \int_{\mathbb{R}^2} e^{2\pi i \{((\vec{\theta}_1 - \vec{\theta}_2) \cdot \vec{r}'_2)\}} \bar{I}(\vec{r}'_2) d\vec{r}'_2 d\vec{\theta}_1 d\vec{\theta}_2. \end{aligned} \quad (\text{A3})$$

Under the assumption of quasi-homogeneity, we can apply van Cittert–Zernike theorem, which relates the intensity distribution at the source  $\bar{I}(\vec{r}'_2)$  with the cross-spectral density function in the far zone  $g(\Delta\vec{\theta})$  via Fourier transform; here we imply that  $\Delta\vec{\theta} = \vec{\theta}_2 - \vec{\theta}_1$ :

$$\langle \phi(\vec{r}_1) \phi^*(\vec{r}_2) \rangle = \iint_{\mathbb{R}^4} e^{-2\pi i \{(\vec{r}_1 \cdot \vec{\theta}_1) - (\vec{r}_2 \cdot \vec{\theta}_2)\}} \sqrt{\hat{I}(\vec{\theta}_1)} \hat{I}(\vec{\theta}_2) g(\Delta\vec{\theta}) d\vec{\theta}_1 d\vec{\theta}_2. \quad (\text{A4})$$

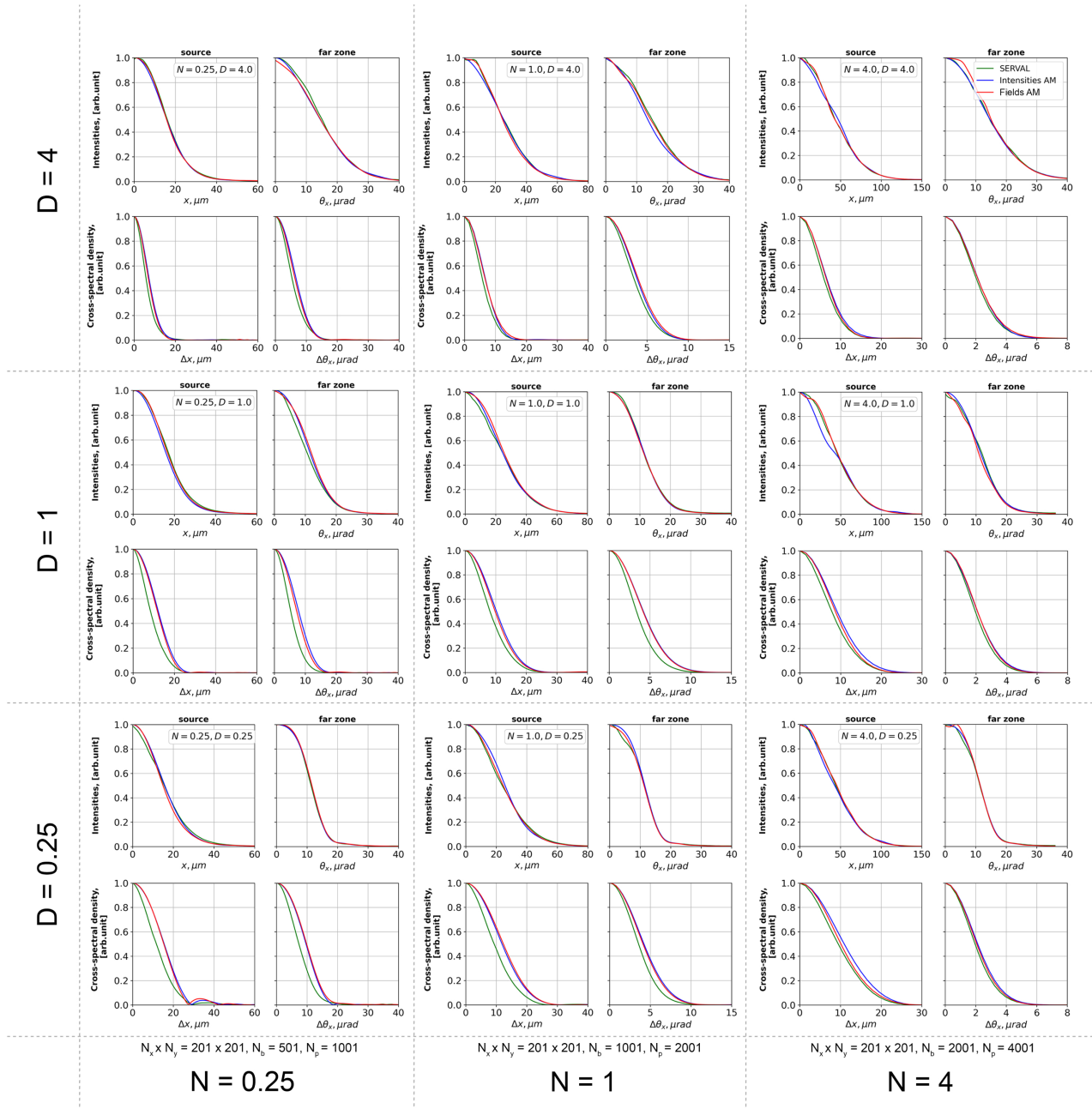


**Fig. 9.** Simulation results with different combinations of  $N$  and  $D$  parameters. In turn, each combination contains results obtained with three methods: SERVAL algorithm (green line), intensity addition method (blue line), and field addition method (red line). For each  $N$  and  $D$  combination, the top rows show *intensity distributions*, bottom rows square moduli of *cross-spectral density functions* for radiation at the *source* location (left columns) and in the *far zone* (right columns). For each  $N$  parameter, we use different numbers of statistical realizations and macroparticles taken, which we mark at the bottom of each column.

Accounting for the relation  $\sqrt{\hat{I}(\vec{\theta}_1)\hat{I}(\vec{\theta}_2)}g(\Delta\vec{\theta}) = \langle \hat{E}(\vec{\eta}, \vec{l}, 0, \vec{\theta}_1)\hat{E}^*(\vec{\eta}, \vec{l}, 0, \vec{\theta}_2) \rangle$  and putting  $\langle \dots \rangle$  outside of the integral, we obtain

$$\begin{aligned} \langle \phi(\vec{r}_1)\phi^*(\vec{r}_2) \rangle &= \left\langle \int_{\mathbb{R}^2} \hat{E}(\vec{\eta}, \vec{l}, 0, \vec{\theta}_1) e^{-2\pi i(\vec{r}_1 \cdot \vec{\theta}_1)} d\vec{\theta}_1 \right. \\ &\quad \times \left. \left( \int_{\mathbb{R}^2} \hat{E}(\vec{\eta}, \vec{l}, 0, \vec{\theta}_2) e^{-2\pi i(\vec{r}_2 \cdot \vec{\theta}_2)} d\vec{\theta}_2 \right)^* \right\rangle \\ &= \left\langle \bar{E}(\vec{\eta}, \vec{l}, 0, \vec{r}_1) \bar{E}^*(\vec{\eta}, \vec{l}, 0, \vec{r}_2) \right\rangle. \end{aligned} \quad (\text{A5})$$

As a result, under the assumption of quasi-homogeneity, SERVAL fixes the correct first order correlation function for the field. Since synchrotron radiation is a Gaussian random process, this is sufficient to fix correlation functions at any order, and therefore to fully define the process.

We now show that the same relation also holds for intensity distributions. Setting  $\vec{r}_1 = \vec{r}_2 = \vec{r}$  in the previous equation, we obtain an expression for intensity distributions at the source in  $(\vec{r})$  domain:

$$\langle \phi(\vec{r})\phi^*(\vec{r}) \rangle = \langle \bar{E}(\vec{\eta}, \vec{l}, 0, \vec{r}) \bar{E}^*(\vec{\eta}, \vec{l}, 0, \vec{r}) \rangle = \bar{I}(\vec{r}), \quad (\text{A6})$$

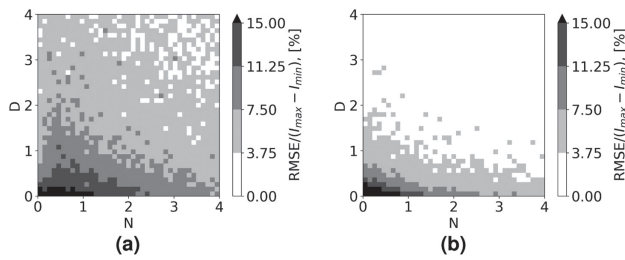


**Fig. 10.** RMSE of cross-spectral density functions of SERVAL and IAM for different sized  $N$  and divergence  $D$  of the electron beam. (a) Cross-spectral density function discrepancy *at the source*. (b) Cross-spectral density function discrepancy *in the far zone*.

and in the same manner, one can show equality for the inverse space domain, i.e.,

$$\langle \hat{\phi}(\vec{\theta}_1)\hat{\phi}^*(\vec{\theta}_2) \rangle = \langle \hat{E}(\vec{\eta}, \vec{l}, 0, \vec{\theta}_1)\hat{E}^*(\vec{\eta}, \vec{l}, 0, \vec{\theta}_2) \rangle, \quad (A7)$$

and when  $\vec{\theta}_1 = \vec{\theta}_2 = \vec{\theta}$ ,

$$\langle \hat{\phi}(\vec{\theta})\hat{\phi}^*(\vec{\theta}) \rangle = \hat{I}(\vec{\theta}). \quad (A8)$$

## 2. Simulations

Here we demonstrate the accuracy of the SERVAL algorithm beyond its strict region of applicability of quasi-homogeneous approximation. This approximation applies when  $N \gg 1, D \gg 1$ . Using SERVAL, IAM, and FAM, we calculate intensity distributions and plot them as well as cross-spectral density functions at both the source and in the far zone. We present results for a combination of  $N, D = 0.25, 1, 4$  in Fig. 9. For the speed test calculation, we use Eq. (33) from [41] for the field in the far zone. As one can see, SERVAL provides correct intensity and cross-spectral density distributions already with  $N = 4$  and  $D = 4$ . Fluctuation of the intensity distributions is caused by a finite number of statistical realizations and macroparticles generated in this simulation.

To illustrate the discrepancy trends, we present a parameter scan of root mean square error (RMSE) between SERVAL and IAM over different combinations of  $N$  and  $D$  parameters. In Fig. 10, each pixel is valued as RMSE, normalized to the factor  $1/(I_{\max} - I_{\min})$  and expressed in percent, where  $I_{\max}$  and  $I_{\min}$  are the maximum and minimum intensities for the IAM result within the simulation window. To facilitate the comparison, the figures are plotted with the same color scale.

These figures show the main trend for the correlation functions: higher  $N$  and  $D$  values provide higher similarity of SERVAL with the intensity addition method results. The intensity distributions coincide exceedingly well for all  $N$  and  $D$  parameters (Fig. 9). As one can see from Fig. 10(a), SERVAL is less applicable for a focused beam. However, the presence of apertures in a focusing system reduces the discrepancy of the cross-spectral density in focus between SERVAL and IAM.

## APPENDIX B: COMPUTATIONAL EFFICIENCY

We compared computational efficiency of the discussed algorithms. Computational time to generate a single statistical realization differs drastically for FAM ( $\sim 670$  ms/realization with 400 macroparticles) and SERVAL ( $\sim 4.2$  ms/realization) on a usual laptop using Python programming language. Here

the transverse mesh consisted of  $201 \times 201$  pixels, with  $N = 4$ ,  $D = 4$ .

IAM does not exploit the concept of statistical realizations. For this method, we performed a test based on a comparison of the time needed to generate an ensemble-averaged (i.e., “weakly monochromatized”) field. We measured the time needed to generate the field presented in Fig. 9 ( $N = 4, D = 4$ ) using SERVAL and IAM. The main criterion for the comparison is that fields should have a sufficient level of convergence with the reasonable number of macroparticles taken: ( $N_p = 4001$ ) for IAM and number of realizations ( $N_b = 2001$ ) for SERVAL. This test showed that SERVAL calculates this field for **11 s** and IAM for **27.6 s**. For memory-saving calculations, one can simulate and propagate each realization or radiation from a macroparticle separately or by chunks (10, 100, … realizations) and store the rest of them on the hard-drive memory, but surely this may significantly slow down a simulation. We note that all three methods are very well suited for parallel computing.

A single SERVAL realization may contain a large amount of spikes. Since each realization is propagatable through the beamline to the sample, one would expect faster convergence at large  $N$  and  $D$ , compared with IAM, which implies propagating a single spike—radiation from each macroparticle—individually.

Comparing SERVAL with the mode decomposition method presented in [20], one can find that with SERVAL, calculation of the  $N_b$  realizations of the field with the mesh grid  $N_g = N_x \times N_y$  starting from noise takes only  $N_b(\mathcal{O}(N_g \log(N_g)) + 2N_g)$  arithmetic operations, where  $\mathcal{O}(\cdot)$  is the big O notation. For the mode decomposition method, calculations require taking  $N_g^2 + N_m$  two-dimensional integrals with the “matrix method”, where  $N_m$  is the number of modes calculated, and with the “two steps method”, it takes  $2N_m N_g(2 + N_m)$  integrations.

## APPENDIX C: DOUBLE-SLIT EXPERIMENT SIMULATION

Here we present the results of a double-slit experiment simulated with SERVAL as well as with the IAM. We exploit parameters similar to those used in the simulation depicted in Fig. 9,  $N = 4$

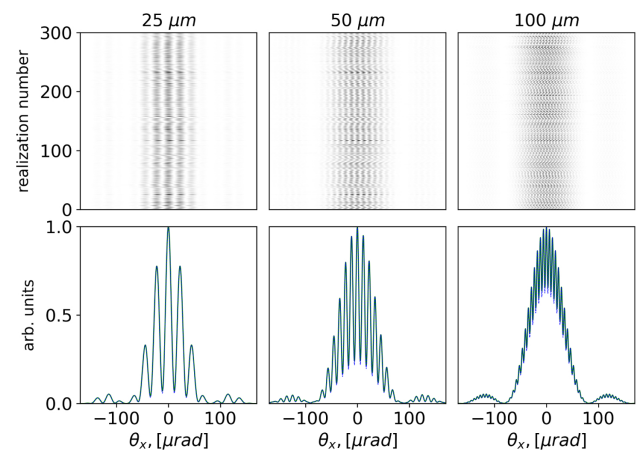


**Fig. 11.** Interference pattern in the far zone after diffraction at the double slits. Two vertical  $8 \mu\text{m}$  slits are located  $25 \text{ m}$  from the source. Slit separation is indicated at the top. SERVAL algorithm, green line; intensity addition method, blue line. The top row represents fringe distribution depending on the realization number for the vertical axis and a transverse distribution obtained with SERVAL for horizontal axis. After averaging over the ensemble, this results in the distributions presented in the bottom row. The approaches show excellent agreement.

and  $D = 4$ . In Fig. 11, we present the simulation result for vertical orientation of the slits.

With SERVAL, we simulate single realizations of partially coherent radiation. Visibility  $\mathcal{V} = (I_{\max} - I_{\min})/(I_{\max} + I_{\min})$  of the diffraction fringes from each realization is equal to unity, which can be seen corresponding to fully coherent radiation. However, this is because each statistical realization is fully deterministic. In other words, it is represented by one given electric field function. To describe a partially coherent source, one needs to collect an ensemble of these statistical realizations to result in statistically meaningful intensities and correlations. By itself, a single realization does not represent the coherence properties of the source.

**Acknowledgment.** We thank Evgeny Saldin for the initial discussions on the realization of the proposed method and his guiding support. We thank Serguei Molodtsov for his interest in this work.

**Disclosures.** The authors declare no conflicts of interest.

**Data availability.** Data presented in this paper are generated with the Ocelot toolkit [33]; the algorithm code described in the paper is publicly available at the dev\_gen development branch of Ocelot and located in ocelot/ocelot/optics/wave.py.

## REFERENCES

- R. Bartolini, "Challenges in the design and construction of diffraction limited synchrotron light sources," presented at DESY Photon Science Users' Meeting (28 January 2021).
- R. Hettel, "Challenges in the design of diffraction-limited storage rings," in *5th International Particle Accelerator Conference (IPAC)*, JACoW, Geneva, Switzerland, 2014, p. 5.
- F. Cerrina, "Ray tracing of recent VUV monochromator designs," *Proc. SPIE* **0503**, 68–77 (1984).
- A. Erko, *Modern Developments in X-Ray and Neutron Optics*, Springer Series in Optical Sciences (Springer, 2008), Vol. 137.
- M. S. del Rio, N. Canestrari, F. Jiang, and F. Cerrina, "SHADOW3: a new version of the synchrotron x-ray optics modelling package," *J. Synchrotron Radiat.* **18**, 708–716 (2011).
- X. Shi, R. Reininger, M. S. del Rio, and L. Assoufid, "A hybrid method for x-ray optics simulation: combining geometric ray-tracing and wavefront propagation," *J. Synchrotron Radiat.* **21**, 669–678 (2014).
- G. Geloni, E. Saldin, E. Schneidmiller, and M. Yurkov, "Transverse coherence properties of x-ray beams in third-generation synchrotron radiation sources," *Nucl. Instrum. Methods Phys. Res. A* **588**, 463–493 (2008).
- Y. Takayama, N. Takaya, T. Miyahara, S. Kamada, W. Okamoto, T. Hatano, R. Tai, and Y. Kagoshima, "Spatial coherence of undulator radiation beyond the van Cittert-Zernike theorem," *Nucl. Instrum. Methods Phys. Res. A* **441**, 565–576 (2000).
- S. Marchesini and R. Coisson, "Spatial coherence of synchrotron radiation," *Recent Research Developments in Optics UCRL-JRNL-200688* (Lawrence Livermore National Laboratory (LLNL), 2003).
- R. Coisson and S. Marchesini, "Gauss-Schell sources as models for synchrotron radiation," *J. Synchrotron Radiat.* **4**, 263–266 (1997).
- R. Coisson, "Spatial coherence of synchrotron radiation," *Appl. Opt.* **34**, 904–908 (1995).
- K.-J. Kim, "Brightness, coherence and propagation characteristics of synchrotron radiation," *Nucl. Instrum. Methods Phys. Res. A* **246**, 71–76 (1986).
- K.-J. Kim, "A new formulation of synchrotron radiation optics using the Wigner distribution," *Proc. SPIE* **0582**, 2–9 (1986).
- J. Goodman, *Statistical Optics*, Wiley Series in Pure and Applied Optics (Wiley, 2015).
- R. Khubbutdinov, A. P. Menushenkov, and I. A. Vartanyants, "Coherence properties of the high-energy fourth-generation x-ray synchrotron sources," *J. Synchrotron Radiat.* **26**, 1851–1862 (2019).
- A. Singer, "Coherence properties of third and fourth generation x-ray sources. Theory and experiment," Technical Report DESY-THESIS-2013-023 (Deutsches Elektronen-Synchrotron (DESY), 2013).
- W.-Q. Hua, F.-G. Bian, L. Song, X.-H. Li, and J. Wang, "Hard x-ray optics simulation using the coherent mode decomposition of the Gaussian Schell model," *Chin. Phys. C* **37**, 068001 (2013).
- W. Q. Hua, F. G. Bian, L. Song, Y. Wang, and J. Wang, "Application of Gaussian Schell-model and its coherent mode decomposition on hard x-ray synchrotron radiation," in *Symposium on Photonics and Optoelectronics* (2012), pp. 1–6.
- A. Singer and I. A. Vartanyants, "Modelling of partially coherent radiation based on the coherent mode decomposition," *Proc. SPIE* **8141**, 814106 (2011).
- M. Glass, "Statistical optics for synchrotron emission: numerical calculation of coherent modes," Ph.D. thesis (Université Grenoble Alpes, 2017).
- R. Li and O. Chubar, "Memory and CPU efficient coherent mode decomposition of partially coherent synchrotron radiation with subtraction of common quadratic phase terms," *Opt. Express* **30**, 5896–5915 (2022).
- O. Chubar, "Synchrotron radiation workshop," 2013, <https://github.com/ochubar/SRW>.
- O. Chubar and P. Elleaume, "Accurate and efficient computation of synchrotron radiation in the near field region," in *European Particle Accelerator Conference* (1998), pp. 1177–1179.
- O. Chubar, Y. S. Chu, K. Kaznatcheev, and H. Yan, "Application of partially coherent wavefront propagation calculations for design of coherence-preserving synchrotron radiation beamlines," *Nucl. Instrum. Methods Phys. Res. A* **649**, 118–122 (2011).
- O. Chubar, L. Wiegert, A. Fluerasu, M. Rakitin, J. Condie, P. Moeller, and R. Nagler, "Simulations of coherent scattering experiments at storage ring synchrotron radiation sources in the hard x-ray range," *Proc. SPIE* **11493**, 1149310 (2020).
- L. Wiegert, M. Rakitin, Y. Zhang, A. Fluerasu, and O. Chubar, "Towards the simulation of partially coherent x-ray scattering experiments," *AIP Conf. Proc.* **2054**, 060079 (2019).
- O. Chubar, M. S. Rakitin, Y.-C. Chen-Wiegert, A. Fluerasu, and L. Wiegert, "Simulation of experiments with partially coherent x-rays using synchrotron radiation workshop," *Proc. SPIE* **10388**, 1038811 (2017).
- L. Wiegart, A. Fluerasu, D. Bruhwiler, and O. Chubar, "Partially coherent wavefront propagation simulations: mirror and monochromator crystal quality assessment," *AIP Conf. Proc.* **1741**, 040013 (2016).
- N. Canestrari, O. Chubar, and R. Reininger, "Partially coherent x-ray wavefront propagation simulations including grazing-incidence focusing optics," *J. Synchrotron Radiat.* **21**, 1110–1121 (2014).
- O. Chubar, L. Berman, Y. S. Chu, A. Fluerasu, S. Hulbert, M. Idir, K. Kaznatcheev, D. Shapiro, Q. Shen, and J. Baltser, "Development of partially-coherent wavefront propagation simulation methods for 3rd and 4th generation synchrotron radiation sources," *Proc. SPIE* **8141**, 814107 (2011).
- O. Chubar, "Simulation of emission and propagation of coherent synchrotron radiation wave fronts using the methods of wave optics," *Infrared Phys. Technol.* **49**, 96–103 (2006).
- S. Reiche, "Numerical studies for a single pass high gain free-electron laser," DESY-THESIS-2000-012 (1999), p. 177.
- "Ocelot," <https://github.com/ocelot-collab/ocelot>.
- M. Yabashi, K. Tamasaku, and T. Ishikawa, "Characterization of the transverse coherence of hard synchrotron radiation by intensity interferometry," *Phys. Rev. Lett.* **87**, 140801 (2001).
- M. Yabashi, K. Tamasaku, and T. Ishikawa, "Measurement of x-ray pulse widths by intensity interferometry," *Phys. Rev. Lett.* **88**, 244801 (2002).
- P. H. van Cittert, "Die Wahrscheinliche Schwingungsverteilung in Einer von Einer Lichtquelle Direkt Oder Mittels Einer Linse Beleuchteten Ebene," *Physica* **1**, 201–210 (1934).
- F. Zernike, "The concept of degree of coherence and its application to optical problems," *Physica* **5**, 785–795 (1938).
- A. Lang, "Simulation of stochastic partial differential equations and stochastic active contours," Ph.D. Thesis (Universität Mannheim, 2007).
- G. Goon, "Cosmic microwave background simulations," GitHub (2021), <https://github.com/garrett361/cmbpy>.
- T. Pfeifer, Y. Jiang, S. Düsterer, R. Moshammer, and J. Ullrich, "Partial-coherence method to model experimental free-electron laser pulse statistics," *Opt. Lett.* **35**, 3441–3443 (2010).
- G. Geloni, E. Saldin, E. Schneidmiller, and M. Yurkov, "Fourier treatment of near-field synchrotron radiation theory," *Opt. Commun.* **276**, 167–179 (2007).